










## Research Article

# Mechanical and Thermal Properties of Calcined Clay Mixed with Agrowaste Char for Sustainable Building Applications

**Benjamin Agyei-Tuffour** <sup>1</sup>, **Michael E. Sewordor** <sup>1,2</sup>, **John Freeman Baffoe** <sup>1</sup>,  
**Martha Forson**<sup>1</sup>, **John Ekow Ampah-Essel**<sup>1</sup>, **Beatrice Ardayfio** <sup>1</sup>, **Bashiru Kadiri-English**<sup>1</sup>,  
**Kwame K. Marfo** <sup>1</sup>, **John Adjah** <sup>1</sup>, **Joshua Tuah Asante** <sup>4</sup>, **Emmanuel Nyankson** <sup>1</sup>,  
 and **David Dodoo-Arhin** <sup>1,3</sup>

<sup>1</sup>Department of Materials Science and Engineering, School of Engineering Sciences, College of Basic and Applied Sciences, University of Ghana, Legon, Accra, Ghana

<sup>2</sup>Department Materials Engineering, Institute of Industrial Research, Council for Scientific and Industrial Research, East Legon, Accra, Ghana

<sup>3</sup>Institute of Applied Science and Technology, University of Ghana, Legon, Accra, Ghana

<sup>4</sup>Department of Metallurgical and Materials Engineering, University of Pretoria, Pretoria, South Africa

Correspondence should be addressed to Benjamin Agyei-Tuffour; bagyei-tuffour@ug.edu.gh

Received 6 February 2024; Revised 28 June 2024; Accepted 2 August 2024

Academic Editor: Necmettin Maraşlı

Copyright © 2024 Benjamin Agyei-Tuffour et al. This is an open access article distributed under the Creative Commons Attribution License, which permits unrestricted use, distribution, and reproduction in any medium, provided the original work is properly cited.

This paper presents a combined experimental and computational result on the mechanical and thermal properties of calcined clay-agrowaste char composites for sustainable building applications. The calcined clays were characterized for their structural, microstructural, mechanical, and thermal properties after they were mixed with 5 wt%, 10 wt%, 15 wt%, and 20 wt% of agrowaste char of varying sources (i.e., coconut, palm kernel, and acacia). Analytical and finite element analyses were used to predict and also confirm the experimentally determined results. The results show that increasing char fractions increases the thermal energy properties but reduces the mechanical properties. For the compressive strength results, it was noted that the palm kernel char composite recorded the highest compressive strength (~4.60 MPa) followed by coconut char (~4.23 MPa) and acacia char composites (~4.14 MPa). The optical micrographs show uniform distribution of the char in the clay/cement matrix. The analytical and finite element analysis predictions show that the sample with microcracks recorded appreciable fracture toughness (~38.2 MPa/mm<sup>-0.5</sup>) and slow rate of energy release during fracture. The implications of the results are discussed to elaborate on the role calcined clays and agrowaste chars plays on the thermal and mechanical properties for a sustainable building materials industry.

## 1. Introduction

The rising cost of energy coupled with increasing energy demands in modern buildings has reached concerning levels recently [1, 2]. This is due to increased use of automation in domestic and commercial buildings, electrical gadgets, air conditioning for cooling and heating, and so on [3, 4]. A prior study shows an ~8.0% increase in electricity demand in Africa annually and ~56% of total energy generated is consumed in buildings [5, 6]. The increased consumption is

due to the type and nature of the building materials used in their construction. Studies into cementitious products such as concretes, and mortars show the enormous efforts at improving energy efficiencies in buildings [7–9]. However, these are largely based on limestone cement, which also contributes to greenhouse gas emissions, hence exacerbating the global warming challenges due to the decarbonization of calcium carbonate, which generates excess carbon dioxide. It is imperative to reduce the carbon footprint related to cement production and explore alternative materials and

manufacturing methods that minimize CO<sub>2</sub> emissions. To address these concerns, it has become crucial to explore alternative approaches. Therefore, the need for an environmentally sustainable material to minimize the energy consumption during the production of limestone cement, as well as reducing the carbon footprint related to cement production, while maintaining thermal comfort in modern buildings cannot be overemphasized. The exploitation of aluminosilicate mineral deposits coupled with nano- and microporous materials from agricultural residues and wastes presents a new paradigm to reaching this new objective. Mixtures of calcined clays and agrowaste chars are able to thermally harvest energy while controlling the rate of heat release [10, 11].

By using calcined clays as raw materials, we can reduce the reliance on traditional cement production methods that contribute to CO<sub>2</sub> emissions. This shift toward sustainable and environmentally friendly practices is essential for the construction industry to mitigate its impact on climate change and work toward a more sustainable future. Additionally, incorporating thermal energy harvesting properties into these cementitious materials can further enhance their sustainability and energy efficiency [12, 13]. Coconut, palm kernel shells, and acacia wood are agricultural wastes commonly available in great quantities in Ghana and tropical Africa. When these agricultural wastes are charred, they enrich the carbon content of the biomass as well as create initial porosities in the material [14–18], thereby enhancing the thermal energy harvesting properties. These pores serve as sites where heat is emitted from the buildings in hot weather as well as allowing cool air into the building in cold weather [10, 19].

This study investigates the potential of producing composite bricks from calcined clay mixed with char made from palm kernel shells, coconut shells, and acacia wood for effective thermal energy harvesting in Ghana. This is in line with introducing new prospects for sustainable construction materials, with a focus on using environmentally friendly and available materials, such as calcined clay and agrowaste. Many researches in this field have used various agrowaste materials, but this paper uses three different agrowaste materials combined with clay obtained from Ghana [15, 17, 20, 21]. The geological location of clay influences the properties of the clay in its application. Rock types exhibit distinct physical, chemical, mineralogical, and mechanical qualities due to the influence of diverse processes such as diagenesis and weathering during their formation and deposition [22]. The study analyzes the composite bricks' heat flow and mechanical properties. In order to analyze various conditions while saving time, finite element analysis (FEA) models were employed to investigate the heat flow and thermal stress distributions using COMSOL Multiphysics software. Finite element analysis (FEA) software can integrate time-dependent mechanical and thermal properties of materials and simulate some responses similar to real-life scenarios while saving time and cost [23, 24].

## 2. Theory

Heat flow in solids and fluids in either one, two, or three dimensions is important in thermal energy storage process in building blocks. Heat transfer usually occurs through conduction, convection, and radiation, and each mode may operate independently or in combination [25–32]. The following equations have been considered when studying heat transfer through different media [33]. During heat flow across and inside of building structures, the mode of heat transfer often varies. Heat is radiated to the surface of the wall, where it is absorbed. The heat is then conducted through the wall and into the indoor air space via convection and finally to the indoor surface through radiation using the following equation:

$$\begin{aligned} Q_{\text{cond}} &= w\rho C_p \Delta T \\ &= Q_{\text{conv}} \\ &= hA(T_i - T_o) \\ &= Q_{\text{rad}} \\ &= A\varepsilon T^4, \end{aligned} \quad (1)$$

where  $Q$  is the heat flow,  $w$  is the thickness of the wall related to equation (2),  $\rho$  is the density,  $C_p$  is the heat capacity, and  $\Delta T$  is the temperature change.

$$w = \sqrt{2\alpha t}, \quad (2)$$

which relates the block thickness to the thermal diffusivity ( $\alpha$ ) and time of exposure ( $t$ ) to the heating source. These then connect to a relationship between thermal conductivity and diffusivity in ways in which the block can quickly conduct the heat and reduce the rate of dissipation. This increases the thermal energy storage in the char-mixed composite block in this study. Equation (1) is then simplified in the following equation:

$$Q = \sqrt{2\alpha t} \Delta T \left( \frac{\lambda}{\alpha^{0.5}} \right). \quad (3)$$

Fourier's law of heat conduction, which is the general heat conduction equation, states that the time rate of heat transfer through a material is proportional to the negative gradient in the temperature and the area, at right angles to that gradient through which the heat flows, and it is given in the following equation:

$$\dot{Q} = -kA \frac{dT}{dx}, \quad (4)$$

where  $\dot{Q}$  is the heat flux or heat flow rate (W/m<sup>2</sup>),  $k$  is the thermal conductivity of the material,  $A$  is the surface or cross-sectional area (m<sup>2</sup>), and  $(dT/dx)$  is the temperature gradient. The negative sign in equation (4) indicates that heat always flows in the direction of decreasing temperature.

The general heat conduction equation considered in the model of the composite brick wall without a heat source inside is given in equations (4) and (5).

$$\left[ \frac{\partial}{\partial x} \left( k \frac{\partial T}{\partial x} \right) + \frac{\partial}{\partial y} \left( k \frac{\partial T}{\partial y} \right) + \frac{\partial}{\partial z} \left( k \frac{\partial T}{\partial z} \right) \right] = \rho C_p \frac{\partial T}{\partial t}, \quad (5)$$

where  $k$  is the thermal conductivity of the material (W/mK),  $T$  is the temperature (K),  $\rho$  is the density of the material (kg/m<sup>3</sup>), and  $C_p$  is the specific heat of the material (J/kg K).  $x$ ,  $y$ , and  $z$  ( $\psi_{w,r}$ ) coordinates are considered for a brick wall. Considering the heat transfer from the inner surface of the building to the inside air is taken to be only convective heat transfer. The boundary condition at the inner surface and outer surface is given in equations (4) and (5), respectively.

$$k \frac{\partial T}{\partial \psi} \Big|_{\psi=0} = 0 + h_i (T_{\psi=0} - T_i) = 0. \quad (6)$$

Heat transfer by conduction, convection, and radiation is considered in the outer surface of a building.

$$k \frac{\partial T}{\partial \psi} \Big|_{\psi=L} = L + h_{\infty} (T_{\infty} - T_{\psi=L}) + \varepsilon \sigma (T_{\text{outside}}^4 - T_{\text{ky=L}}^4) = 0, \quad (7)$$

where subscript  $\infty$  represents ambient,  $h$  is the convection heat transfer coefficient,  $\varepsilon$  is the emissivity, and  $\sigma$  is the Stefan–Boltzmann constant. The simulation assumed time-dependent temperature distributions and also the variable temperature of inside air and outside air, and the studied problem was solved as nonstationary heat transfer to describe these processes [34]:

$$\rho C_p \frac{\partial T}{\partial t} + \rho C_p \mathbf{u} \cdot \nabla T = \nabla \cdot (k \nabla T) + Q. \quad (8)$$

### 3. Materials and Methods

**3.1. Materials Preparation.** The aluminosilicate minerals in Ghana are the industrially exploited secondary clay deposit in Ghana. The clay was crushed and dried in an oven at 105°C to remove volatile compounds and moisture. The dried clay was then pulverized and calcined in a gas kiln at 750°C for 60 minutes at a rate of 5°C/mins and cooled to room temperature. The transformed clay before and after processing is shown in Figures 1(a) and 1(b), respectively.

The mineralogical composition of the raw and calcined clay was analyzed using the X-ray fluorescence spectroscopy (XRF) and X-ray diffraction techniques (XRD). XRF analysis was carried out using a Thermo Fisher ARL9400 XRF system and Win XRF software for data interpretation. The analysis was performed by stimulating the samples with a primary X-ray source and measuring the resulting fluorescence emitted from the sample. The XRF analyzer was used to establish the chemistry of the raw and calcined Abonko clays. During the scan in an XRF, each element present emits a distinct set of fluorescent X-rays that are unique to that element. Also, XRD analysis was conducted using theta/theta goniometry and operating at 35 kV and 50 mA. XRD was used to determine the crystallographic structure and phase identification of the raw and calcined clays. A continuous scan from  $2\theta = 5.05^\circ - 99.87^\circ$  with a step size of  $0.105^\circ$  and a scan step

time of 47.68 s was performed to identify the phases after which the phase analysis was carried out using a Philips XPERT-PRO HighScore plus search software.

The functional groups and bond structures between the various raw and carbonized agrowastes, as well as the raw and calcined Abonko clay, were performed using the Bruker Opus-7.5.18 (Bruker, France) Fourier transform infrared spectrometer (FTIR) to analyze the test samples. These measurements were performed in the transmittance mode with a scan range of 400–4000 cm<sup>-1</sup> using 16 scans, and the data obtained were plotted into a transmittance spectra using Origin software.

The heat content and thermal degradation analyses were performed using the SDT Q600 V20.9 Build 20 thermogravimetric and differential scanning calorimetric (TGA-DSC) system. For this test, ~5–10 mg of each specimen was placed in an alumina (Al<sub>2</sub>O<sub>3</sub>) crucible and exposed to a direct heating ramp at a rate of 10°C/min from 20°C to 900°C using nitrogen as the purging gas. The weight loss and heat content as a function of temperature were recorded, and the data were plotted using origin graphing software. The surface morphology, phase separation, and texture were investigated using a focused beam of electrons directed at the sample to produce a complex, high magnification image of the sample's surface topography. A compound AmScope microscope with MD 130 lens was used to observe the morphological properties of the composites. The MD 130 eyepiece lens has a maximum resolution of 1280 × 1024 and 1.3 MP live color image, and the 2-objective eyepieces have a magnification of WF 10X/20. The lens was attached to the trinocular port on the microscope to aid in transferring images to the camera for viewing on the computer monitor.

The specimen for analysis was placed directly over the circle of light. While operating the microscope, the light intensity was adjusted appropriately to achieve the quality images. It is important to note that low-intensity light allows for more details to be visible and high-intensity light gives a washed-out appearance. The reflective mode analysis was carried out on the specimen with the help of the coarse and fine focus knob, which fine-tunes the image for a capture.

**3.2. Carbonization of Coconut, Acacia, and Palm Kernel Shells.** Ten kg each of coconut shells, acacia, and palm kernel shells was air-dried, carbonized, and activated in a furnace at ~700°C at a heating rate of ~4°C/min. The particle sizes of the carbonized shells were sieved through a 1 cm × 1 cm mesh. Figures 1(c), 1(d), 1(e), 1(f), 1(g), and 1(h) show the transformation of the agrowastes into char.

**3.3. Composite Preparation and Batch Formulation.** The calcined Abonko clay, GHACEM cement (32.5 R), and carbonized agrowaste char were used in the composite fabrication. The calcined clay is used to improve the pozzolanic reactions and cement as the original binder and the carbonized materials to aid in thermal energy harvesting. Tables 1 and 2 present the batch formulations for the cubes and rectangular bars fabricated (Figures 1(i), 1(j), and 1(k)) for testing. It is important to note that three different



FIGURE 1: Photographs of (a) raw Abonko clay, (b) calcined Abonko clay, (c) acacia wood, (d) coconut shells, (e) carbonized coconut shells, (f) carbonized acacia wood, (g) palm kernel shells, (h) carbonized palm kernel shells, (i) fabrication process of samples, (j) compression test, and (k) flexural test.

TABLE 1: Batch formulation for cubes.

Item	Control	5% addition	10% addition	15% addition	20% addition
Calcined clay (g)	150.0	150.0	150.0	150.0	150.0
Cement (g)	37.5	37.5	37.5	37.5	37.5
Carbonized material (g)	—	7.5	15.0	22.5	30.0
Water (ml)	67.5	67.5	67.5	67.5	67.5

TABLE 2: Batch formulation for rectangular bars.

Item	Control	5% addition	10% addition	15% addition	20% addition
Calcined clay (g)	100.0	100.0	100.0	100.0	100.0
Cement (g)	25.0	25.0	25.0	25.0	25.0
Carbonized material (g)	—	5.0	10.0	15.0	20.0
Water (ml)	45.0	45.0	45.0	45.0	45.0

carbonized materials were used, and hence, a total of thirteen compositions were made. The first composition served as the control sample which was without carbonized materials, and the other twelve were with varying percentages of carbonized materials. The ratio of calcined clay to cement was 4 : 1 and 31% of water.

**3.4. Briquettes Production.** The various materials were weighed in accordance with the batch formulation and mixed manually until a homogenous mix was obtained before the specific amount of water was added. The mixture was transferred into the lubricated mold box of 50 mm<sup>3</sup> dimensions and joggled for a minute. The cast was then left

to dry for 24 hours at room temperature, demolded, and further dried at 105°C in a CJ-9053A laboratory dry oven for 24 hours. Five samples were produced for each formulation. Figure 1(i) shows the fabrication process of the cubic and rectangular bar briquettes.

**3.5. Mechanical Properties of Briquettes.** The mechanical characteristics of the samples were determined by measuring the compressive strength and modulus of rupture (flexural strength) as shown in Figures 1(j) and 1(k).

The force applied and displacements were recorded to determine the compressive strengths. The process was carried out following BS EN 196-1:2016 standard.

The bar was positioned exactly at the middle of the rollers of the equipment, closed, and the parameters inputted using the MOR/5-TS system. The load was applied and the load that fractures the sample is recorded, and the bending strength is calculated. Figure 1(k) shows the MOR machine and a rectangular bar that has been tested.

**3.6. Analytical and Finite Element Modeling.** To better comprehend the interplay between the loads applied and the different agrowaste char-calcined clay test materials, finite element modeling (FEM) uses the COMSOL Multiphysics software. Meshing was done using a four-node elemental mesh and ensured fine meshes were used in areas where high-load interaction was perceived. To ensure a stable simulation, the top and bottom boundaries were fixed and uniform load was applied to the midsection. The stress distribution of the steel material was estimated using the von Mises stress-yielding criterion.

## 4. Results and Discussion

**4.1. Composition and Structural Analyses of Clay Samples.** Table 3 and Figures 2(a), 2(b), 2(c), 2(d), and 2(e) present the X-ray fluorescence (XRF) and X-ray diffraction (XRD) analyses from the raw and calcined clay showing that they are composed of kaolinite and rich in quartz composition having a high content of iron oxide and appreciable amounts of potassium and titanium oxide. Upon calcination, the clay increased in quartz, potassium, titanium, iron, and magnesium oxides as confirmed by findings reported in literature [35–39]. On the behavior of kaolinitic clays calcined above 600°C, the presence of the oxides assists in the formation of glassy phases that improve the mechanical properties of the calcined clay [40]. The XRD analysis report in Figure 2(a) shows the crystallography structure and the phases present in the raw and calcined clays at 750°C. Both clays have two distinct patterns present; kaolinite ( $\text{Al}_2\text{O}_3 \cdot 2\text{SiO}_2 \cdot 2\text{H}_2\text{O}$ ) and quartz ( $\text{SiO}_2$ ) with similar peak positions and intensities for the quartz phases were observed in the raw and calcined clay, but different in the kaolinite peaks. The calcined clay showed missing kaolinite phases as well as great reduction in intensities compared with the raw clay. This is confirmed by Kwakye-awuah et al. [41], who report that existing kaolinite peaks or reflection at (010) and (020) is lost when kaolin is calcined. Similar observations of reduced intensities were made by Akolekar [42] and Kovo [43] for quartz peaks present in the calcined clay. The Fourier transform infrared spectroscopy (FTIR) analysis displayed in Figures 2(b), 2(c), 2(d), and 2(e) reveals the distinct absorption peaks indicative of the molecular composition of the sample. These peaks, corresponding to specific functional groups, provided valuable insights into the chemical structure of the control sample and the bio-based chars. The O-H bond ( $\sim 2100\text{--}2324\text{ cm}^{-1}$ ) and C≡C bond ( $3397\text{ cm}^{-1}$ ) represent the hydroxyl and alkyne groups, whereas  $\sim 1600$  and  $600\text{ cm}^{-1}$  represents the carbonyl, alkene, and alkane groups. The palm kernel-clay composite shows the presence of seven peaks. The C≡C triple bond at  $2182\text{ cm}^{-1}$  in the composite signifies the presence of hydroxyl (O-H), a hydrogen bond detected at

TABLE 3: XRF analysis of raw and calcined Abonko clay.

Oxides	Raw Abonko clay (%)	Calcined Abonko clay (%)
SiO <sub>2</sub>	45.35	64.74
Al <sub>2</sub> O <sub>3</sub>	30.90	20.82
K <sub>2</sub> O	0.62	1.24
NaO	0.75	1.38
CaO	0.07	0.01
TiO <sub>2</sub>	0.64	0.78
MnO	0.02	0.05
Fe <sub>2</sub> O <sub>3</sub>	4.94	7.03
P <sub>2</sub> O <sub>5</sub>	0.02	0.00
SO <sub>3</sub>	0.22	0.11
LOI	16.47	—
Total	<b>100</b>	<b>96.16</b>

The calcined samples contain no volatile components which reports as LOI in the raw Abonko Clay. It shows that after calcination,  $\sim 96.16\text{ wt}\%$  is obtained which is good for the task to be used for.

$3373\text{ cm}^{-1}$ . This follows with research done by Bediako et al. [36] that vibration bands at  $3373\text{ cm}^{-1}$  conform to a metal bonded to a hydroxide group. The C=C bond at  $777\text{ cm}^{-1}$  is a hexagonal form of charcoal representing the presence of char in the composite, and the C=O bond at  $2050\text{ cm}^{-1}$  indicates the presence of a carbonyl group. The single bond (C-H, C-O, and O-H) vibration bands were detected at  $\sim 428\text{ cm}^{-1}$ ,  $\sim 1010\text{ cm}^{-1}$ , and  $\sim 3349\text{ cm}^{-1}$ , respectively. The C=C bond detected at  $\sim 776\text{ cm}^{-1}$  is a hexagonal charcoal form, confirming char's presence in the composite. The triple bond at  $\sim 2081\text{ cm}^{-1}$  affirms the hydroxyl (O-H) hydrogen bond at  $\sim 3349\text{ cm}^{-1}$ . Figure 2(e) shows the results of the acacia char composite. The composite is characterized by a strong band at  $\sim 3374\text{ cm}^{-1}$ , while several peaks with variable intensities were observed at  $\sim 2324$ ,  $\sim 2050$ ,  $\sim 1981$ ,  $\sim 1416$ ,  $\sim 1010$ ,  $\sim 874$ ,  $\sim 775$ , and  $\sim 428\text{ cm}^{-1}$ .

**4.2. Thermal Characteristics of Agrowaste Char-Clay Composites.** The weight loss, heat content, and heat transport properties in the calcined clay-char composites are presented from the thermogravimetric analyzer coupled with differentials scanning calorimetry (TGA-DSC). The samples were heated to 900°C at a scanning rate of 10°C/minute to determine their thermal stability and heat storage characteristics. Figure 3(a) represents the percentage of weight loss for the control and 5–20 wt% addition of coconut char composite as they were heated from RT to  $\sim 900^\circ\text{C}$ . The weight losses for the control sample and 5–20 wt% char samples were 5.9%, 25.4%, 6.9%, 11% for the control, 7%, 6.2%, 7.3%, 10.4% for Pk char composites, and 5%, 7.9%, 8.6%, 10.5% for the Ac char composites. The average losses are also  $\sim 12.6\%$ ,  $\sim 9.1\%$ , and  $\sim 8\%$ , respectively. The losses are due to the breaking of chemical bonds and decomposition as the temperature increases [44]. These results show a decrease in moisture content, decarbonization, dehydration, dehydroxylation, and transformation from amorphous to crystalline state as confirmed by P.E. Grattan-Bellew and Fernandez et al. in prior studies [35, 45]. The agrowaste char samples experienced the evaporation of

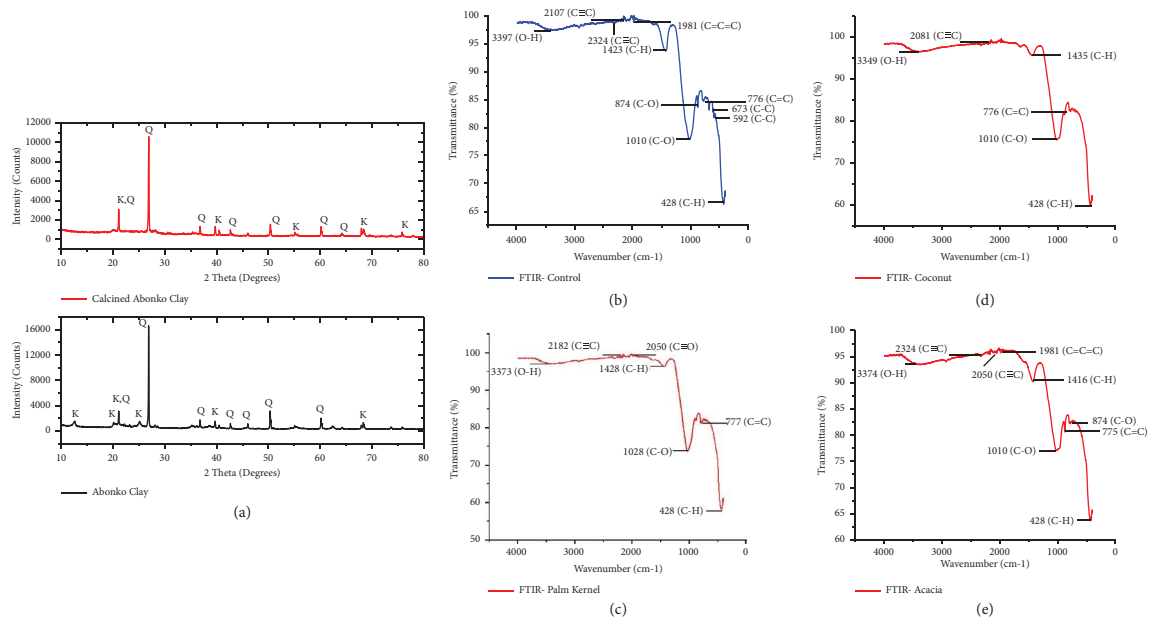


FIGURE 2: (a–e) Structural and functional analyses of aluminosilicates and agrowaste materials: (a) XRD diffractograms of raw and calcined clay and FTIR spectra of (b) control composite, (c) palm kernel char, (d) coconut shell char, and (e) acacia char composite.

water, cement dehydration, clay dehydroxylation, and calcium carbonate decarbonization. However, the weight loss recorded for the control sample was negligible and therefore much more thermally stable.

Conclusively, the highest weight loss recorded was 25.4% from 5% addition of coconut char-calcined clay composite, whereas the lowest recorded was 5% from 5% addition of acacia char-calcined clay composite. The control recorded a 5.9% weight loss. There was no trend in the reduction of coconut char-calcined clay composite samples; however, the palm kernel char- and acacia char-calcined clay composite samples recorded an increase in weight loss with an increase in the addition of char.

The DSC results provide data on the ideal behavior of the material as it is heated. Figure 3(a) shows the thermal behavior of the coconut char composite. At about 200°C and 395°C, an exothermic reaction occurred, and this can be associated with crystallization [46]. Above 410°C, the sample began to absorb heat which may be due to a change in the amorphous material and that accounts for the high percent of weight loss between 400 and 900°C. It is interesting to note that around 680°C another endothermic reaction took place, and this may be due to glass transition. At 900°C, the sample was absorbing –14 mW heat.

The heat content of the coconut, palm kernel, and acacia char composites was investigated with differential scanning calorimetry (DSC) and is presented in Figures 3(d), 3(e), and 3(f). The samples exhibited exothermic reaction (~5 mW and ~11 mW) at ~599°C and 200°C and endothermic peaks among ~505°C, ~520°C, ~325°C, and ~128°C, respectively. These are linked to desorption and change in crystal structure with the heat flow of ~37 mW and –42 mW.

The exothermic reaction at 200°C can be attributed to crystallization whereas the endothermic can be linked to glass transitioning [47]. The acacia char composite samples

exhibited rapid changes for both endothermic and exothermic reactions. Exothermic reactions are attributed to the conformational energy as a result of chemical reactions or the rearrangement of the molecules. Endothermic reactions in the acacia char samples saw rapid temperature changes leading to for the unusual trend in reactions, and this may be related to the energy required for a phase change in the samples. However, the heat flow from the DSC gives a vivid confirmation of the corresponding weight losses recorded in the TGA results in the palm kernel and acacia char composites as shown in Figures 3(e) and 3(f).

**4.3. Microstructural Properties of Samples.** Figures 4(a), 4(b), 4(c), 4(d), 4(e), 4(f), 4(g), 4(h), 4(i), 4(j), 4(k), 4(l), 4(m), and 4(n) show the optical micrographs at a magnification of 20x of the cross section and surface of the composites with 5 wt%, 10 wt%, 15 wt%, and 20 wt% char from coconut, palm kernel, and acacia wastes, respectively. The circled portions of the image show a homogeneous mix of calcined clay and Portland cement in the internal section, oval region shows the presence of iron oxide from the calcined clay material, triangular region represents quartz from the clay, and pentagon-bound area shows pores within the composite. The microcracks in the cross section can be due to the compressive strength test conducted on the sample. The presence and spread of palm kernel char within the matrix of the composite in Figures 4(a), 4(b), 4(c), and 4(d) may have contributed to the good thermal energy harvesting characteristics and compressive strengths of the composite as observed in the TGA-DSC and mechanical property results. The micrographs also show an increase in the quantity of char from Figures 4(e), 4(f), 4(g), and 4(h), and this corroborates the composition and explains the low compressive strength values recorded due to low density of the chars and defects created within the composite.



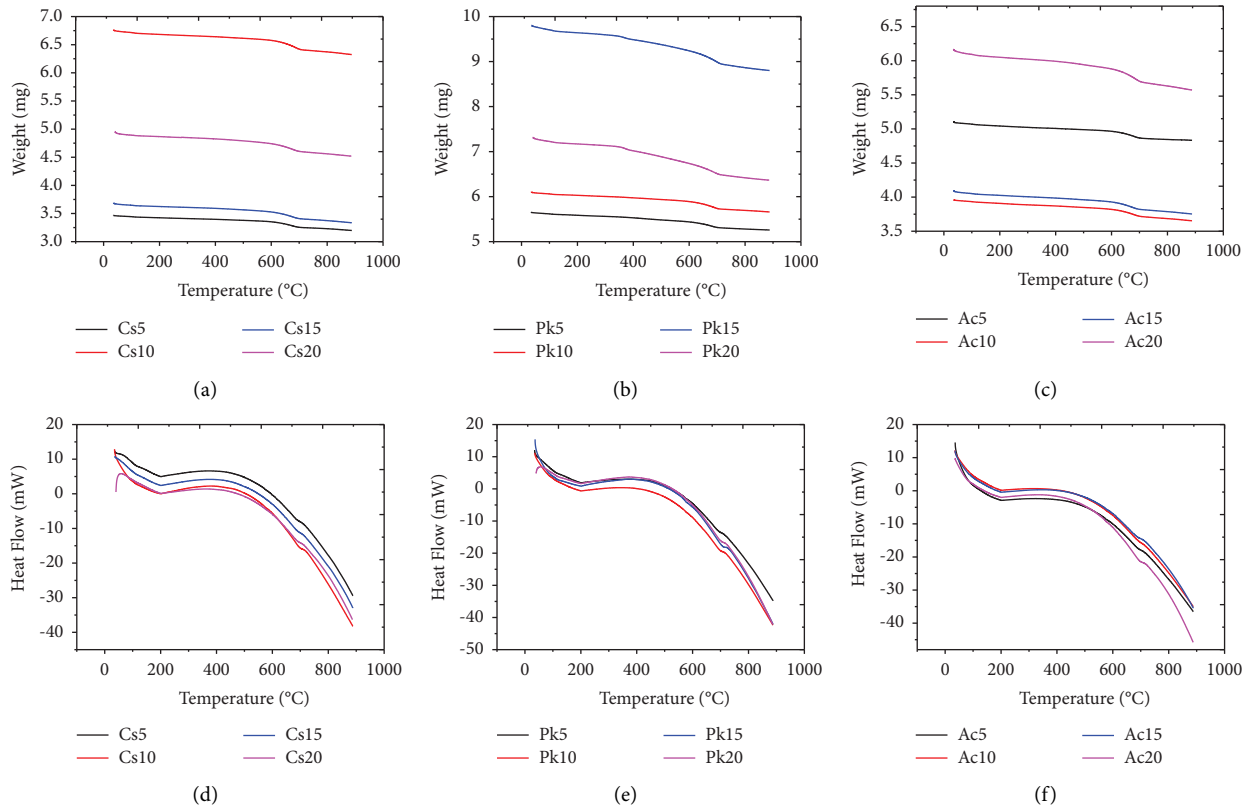


FIGURE 3: Thermogravimetric and differential scanning calorimetry analysis of (a) coconut shell char composite, (b) palm kernel char composite, and (c) acacia char composite and the heat flow in (d) coconut char, (e) palm kernel, and (f) acacia char composite.

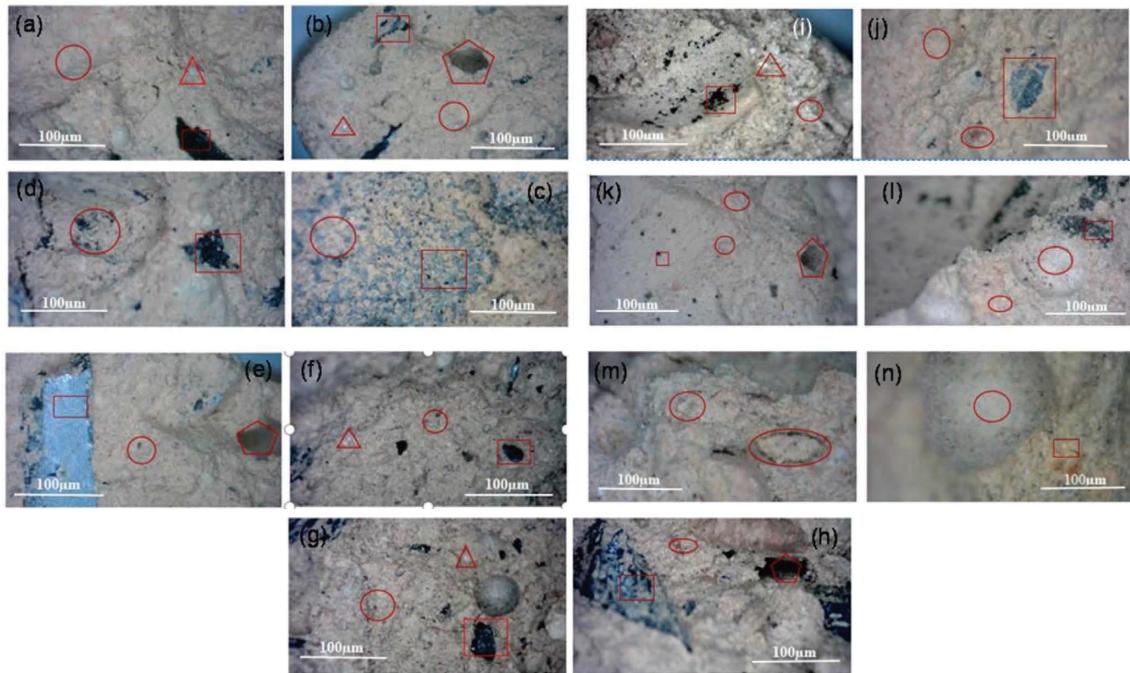


FIGURE 4: (a–n) Cross section and surface microstructural analyses of the 5 wt%, 10 wt%, 15 wt%, and 20 wt% of coconut (a–d), palm kernel (e–h), acacia char (i–l), and the control sample (m, n). (a) Cross-sectional area and (b) surface of the composite.

It can also be observed that the composite is homogeneously mixed; however, a few porous were present in the composite that might contribute to the low strength value of the composite. The char is dispersed within the clay-cement matrix. The presence of char and its high content as the ratio increases confirms the good thermal energy harvesting characteristics and low compressive and flexural strength of the composite, respectively. According to reports, biochar products contain many pore structures which provides vast benefits in the application of energy-saving buildings. Composites of biochar from the agrowaste and calcined clay are known as phase change materials which store as well as release significant amount of latent heat through the phase change process [48]. Also, according to Sachini et al. [21], the pores in the cement-based biochar product have the tendency of stopping thermal bridging within the product, therefore enhancing the thermal insulation, humidity control, and reducing thermal conductivity [20, 49]. Thermal parameters such as specific heat capacity ( $C_p$ ) and thermal conductivity have a great effect on the internal temperature, heating rate, and heat balance of products produced from biochar. Specific heat capacity ( $C_p$ ) indicates the ability of the material to absorb or dissipate heat while thermal conductivity relates to the heat transfer ability and therefore can be related to physical structures such as density, moisture content, and pore characteristics. From research, the specific heat capacity of coconut char, wood char, and palm kernel char is ~between 1640 and 3790 [50], 688 and 2532.85 J/kg/K [51], and 1983 J/kg/K, respectively, while their thermal conductivity of palm kernel char is reported to be 0.68 W/m/K [52]. From the data obtained from literature, it was observed that averagely, coconut char showed the highest specific heat capacity followed by wood char and palm kernel char. Since specific heat capacity indicates the ability of the material to absorb or dissipate heat, it is then assumed that coconut char products will absorb or dissipate heat effectively than wood char products and palm kernel char products.

#### 4.4. Mechanical Response of Agrowaste Char-Clay Composites.

Figures 5(a), 5(b), 5(c), 5(d), and 5(e) present the mechanical properties of the calcined clay-char composites in comparison with the control sample. The compressive strength for the control sample is 7.61 MPa. From Figure 5(a), it can be observed that the control sample recorded a higher compressive strength than all of the agrowaste char composites. Upon comparing the compressive strengths of palm kernel, coconut, and acacia char composites with varying contents (5 wt%, 10 wt%, 15 wt%, and 20 wt %), the palm kernel char composites recorded strengths of ~4.60, ~4.23, ~4.14, and ~3.03 MPa, respectively. That of the coconut char composites recorded were ~3.40, ~2.94, ~2.48, and ~2.39 MPa, respectively. Figure 5(c) presents that of the acacia char composites; the 5 wt.% recorded a compressive strength above the minimum compressive (3.5 MPa) for masonry block.

Generally, the reduction in compressive strength can be attributed to the porous nature of the char content in the composite. Since the char is very porous, they fracture easily

when load is applied to the blocks, hence the lower compressive strength [53, 54]. In addition to reducing the density of composites, biochar also has the propensity for increased water absorption due to the influence of its pores. Consequently, increasing the quantity of biochar promotes the water absorption capacity during the production of the composites. The water contained within the pores of the biochar can serve as nucleation sites for hydration products, resulting in the formation of denser composites with smaller amounts of biochar added [48]. When the volume of hydration products in the pores is smaller than the pore diameters formed by the biochar, the composite becomes porous and results in a reduction in strength [20]. It can then be deduced from the compressive strength results that the optimum amount of char that can be added is 5 wt%. Increasing the char content above 5 wt% is detrimental to the compressive strength required for masonry brick as a result of the increase in pores within the matrix as the char increases.

To compare the flexibility of the composite bricks, the bending test using 3D bend technique was done and the results are presented in Figures 5(d), 5(e), and 5(f). It can be observed that 5 wt% palm kernel char composite had the highest flexural strength of ~1.04 kg/mm<sup>2</sup> among the other char composites and that of the control sample was ~0.53 kg/mm<sup>2</sup>. On the other hand, the flexural strength of the palm kernel composites decreased from 1.04 to 0.33 kg/mm<sup>2</sup> as the content of palm kernel char increased. It can therefore be deduced that the volume of the palm kernel char had a significant effect on the flexural strength. The control sample for the coconut shell char composite had the highest flexural strength of 0.53 kg/mm<sup>2</sup>, and the flexural strength of coconut shell composites decreased as the char increased from 5 wt% and remained constantly at ~0.17 kg/mm<sup>2</sup> for char contents 10 wt%, 15 wt%, and 20 wt% as shown in Figure 5(e).

The flexural strength results of the control and acacia composites are shown in Figure 5(f). It is evident from the graph that the acacia composites' flexural strength reduced marginally from 0.36 kg/mm<sup>2</sup>, 0.35 kg/mm<sup>2</sup>, and 0.31 kg/mm<sup>2</sup> for the 5 wt%, 10 wt%, 15 wt%, and 20 wt%, respectively.

#### 4.5. Finite Element Analysis (FEA) of Agrowaste Char-Calcined Clay Composites.

In order to understand the flexural and compressive behaviors of the composite samples, finite element analyses use the complete Abaqus environment software to model the respective compositions under flexural and compressive loads with 5–20 wt% additions of coconut, palm kernel, and acacia chars.

The presence of microcracks and their influence on the fracture toughness and the energy release rates are the different char. The composite samples exhibit varying fracture toughness with compositions of char and calcined clays.

Figures 6(a), 6(b), 6(c), 6(d), 6(e), 6(f), 6(g), and 6(h) present the thermal stress distributions for the control, palm kernel, coconut shell, and acacia char composites showing



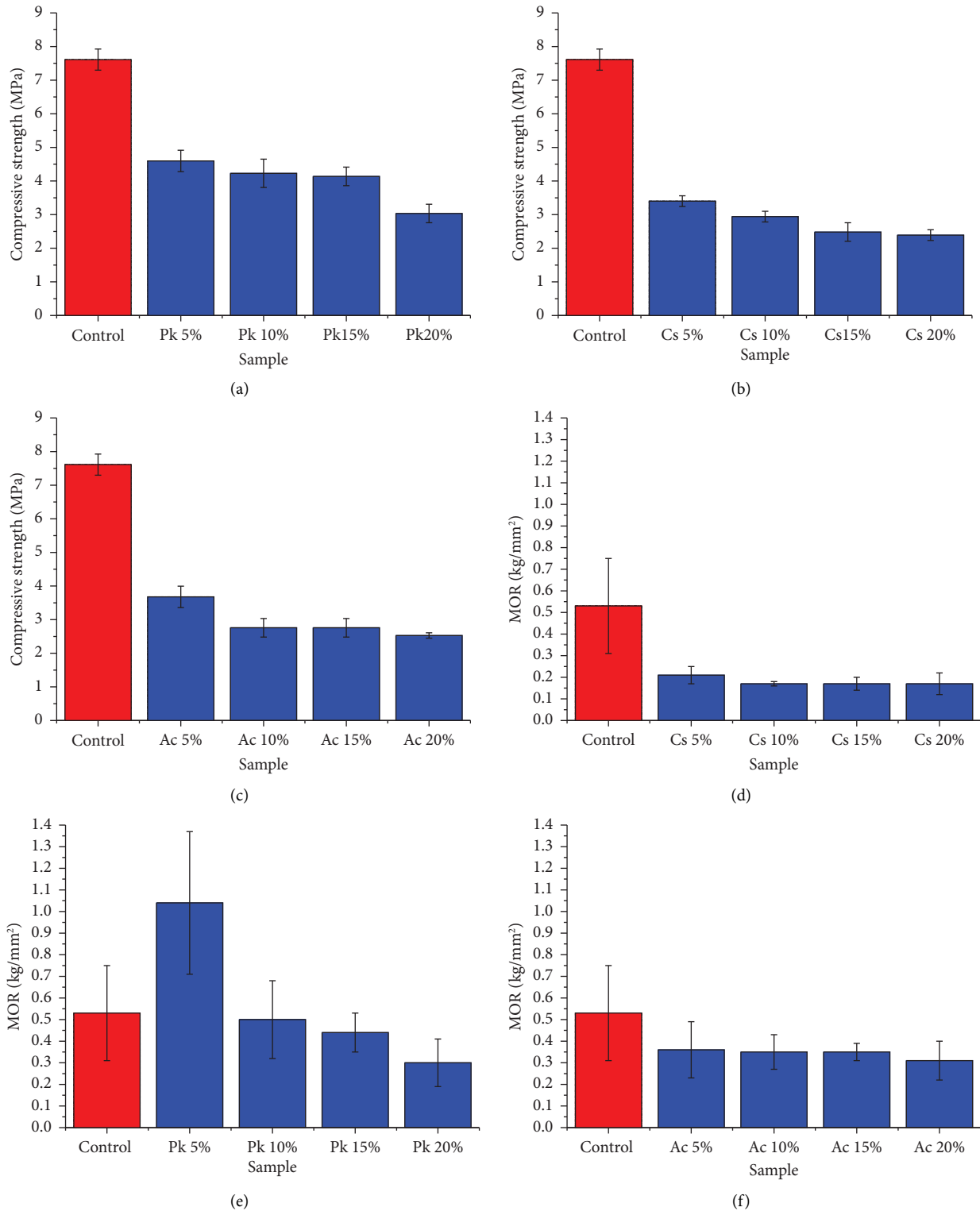


FIGURE 5: Compressive strength results for (a) palm kernel char composite, (b) coconut shell char composite, and (c) acacia char composite and flexural strength results for (d) palm kernel char composite, (e) coconut shell char composite, and (f) acacia char composite.

the surface and volume temperatures. Figure 6(a) represents the control sample in a time-dependent mode after 12 hours of heating the surface and volume temperature of the brick, while Figure 6(b) is the isothermal heat flow for the control

composite. For the exterior surface of the brick, a temperature of 37°C (310 K) was recorded and 29°C (302 K) for the interior surface. A temperature difference of ~8°C implies that heat traveled faster on the outer surface than the inner

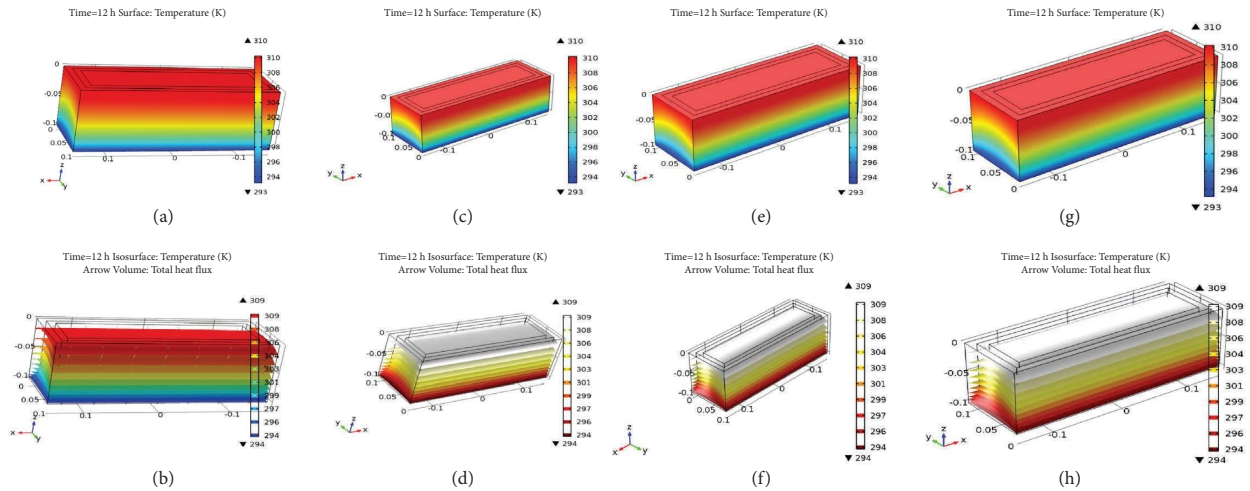


FIGURE 6: Mechanical and thermal stress distributions for (a, b) control, (c, d) palm kernel, (e, f) coconut shell, and (g, h) acacia char composites.

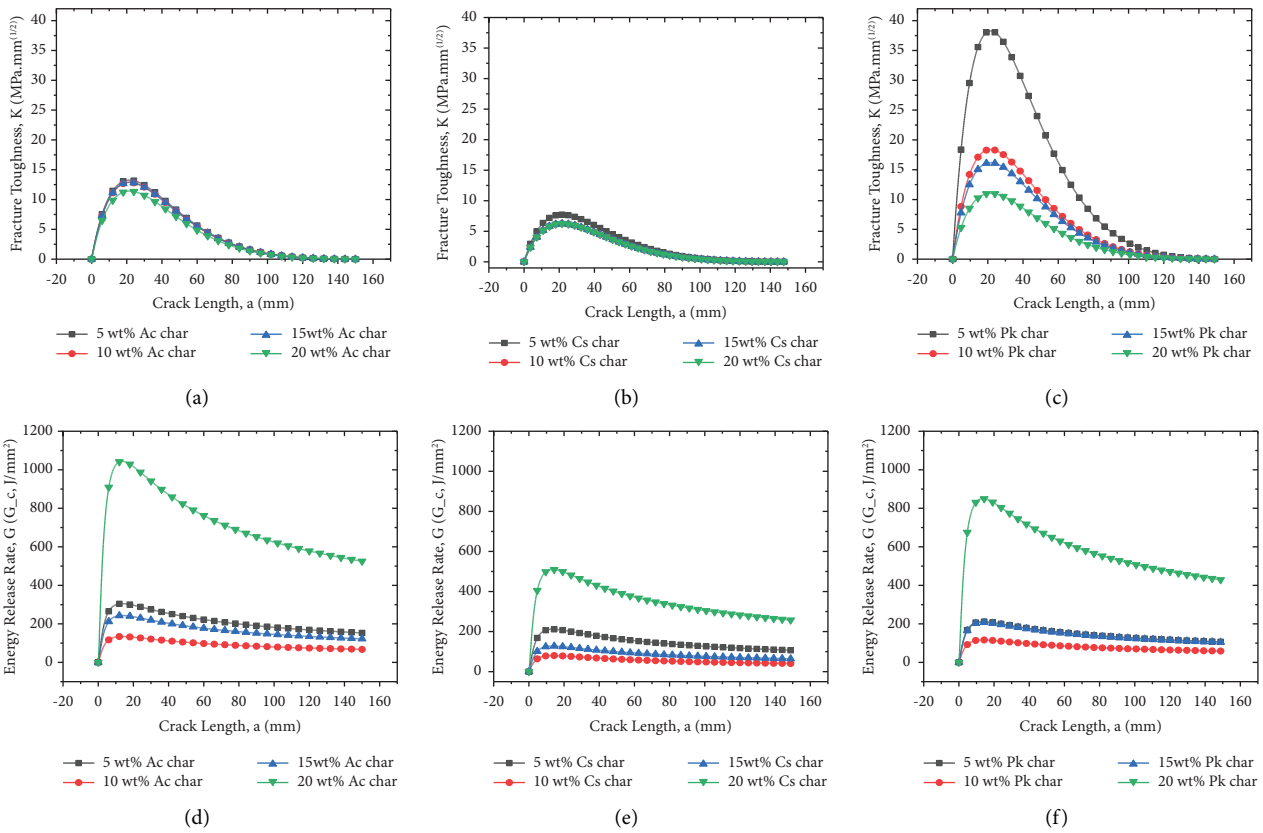


FIGURE 7: Fracture toughness and energy release rate from FEM.

surface, indicating that the brick is much thermally stressed since that part is in direct contact with the heat source. As heat is transferred through the brick via conduction, the heat transfer becomes proportional to the temperature gradients in the system. The simulation shows that the control sample has a high heat transfer rate in the inner surface of the brick.

Figures 6(c) and 6(d) are a 3D image showing the outer temperature profile and the inside temperature distribution in the palm kernel-calcined clay composite material. The surface temperature was 37°C (310 K), and the backside recorded 23°C (294 K) showing a difference of 14°C. The results show that a conductive and comfortable

room temperature can be maintained. The reduction in temperature can be attributed to the characteristics of the palm kernel-calcined clay composite materials. Considering the composite brick model for building applications, the side of the brick with a higher thermal temperature will be directed toward the outside of the building, exposing it to the sun. As the sun shines on the surface of the brick, the temperature rises, and the heat is conducted through the brick. The heat transfer is proportional to the temperature gradients in the system; hence, the room temperature will be lower thereby creating thermal comfort. Thermal comfort occurs due to the transfer of heat to the indoor air via convection and to the indoor surfaces via radiation. From Figure 6(c), it can be observed that parts of the brick are indicated with different colors, illustrating how thermally stressed the region of the composite brick is. Figure 6(d) is the isothermal heat flow of the palm kernel char composite.

The surface and volume temperature for the coconut shells-calcined clay-cement composite is shown in Figures 6(e) and 6(f). Figure 6(e) shows the surface temperature and volume temperature of the brick, while Figure 6(f) shows the isothermal heat flow at 37°C. The study of the model is time-dependent, and the simulation was done for 12 hours. The face of the brick recorded 37°C (310 K) whilst the back recorded 21°C (294 K). A temperature difference of 16°C was recorded for coconut char composites. The outer surface showed high temperatures, while the interior surface recorded reduced temperatures; the outer surface of the brick is more thermally stressed due to direct exposure to the sun. This thermal comfort occurs due to the energy harvesting characteristics of the composite brick. It can be seen that the brick underwent increased thermal stress resulting in fissures and cracks on the sides of the brick (Figure 6(e)).

Figure 6(g) represents the surface temperature composite and (h) the isothermal heat flow of the acacia char. A temperature of 37°C and 21°C was recorded for the exterior and interior surfaces, respectively. The results showed that heat transfer from the exterior to the interior for the acacia char composite was slower compared to the other composites. This can be attributed to the lower thermal conductivity of the acacia char ( $\lambda = 0.0946 \text{ Wm}^{-1}\text{K}^{-1}$ ) [55], hence the ability of the composite to attain thermal comfort. In order to predict the composite's resistance to crack under thermal and mechanical stresses, the mode I fracture toughness ( $K_{IC}$ ) and the rate of crack opening are shown in Figure 7. The peak fracture toughness is shown in Figures 7(a), 7(b), and 7(c) of Pk char sample. The acacia char (20 wt%) recorded the least resistance to crack propagation, hence, an increase in the energy release rate (10.7 MJ/m<sup>2</sup>). The critical crack length of ~20 mm and maximum  $K_{IC}$  (37.5 MPa  $\sqrt{\text{mm}}$ ) for palm kernel were recorded. The corresponding  $G_c$  of ~10.7 MJ/m<sup>2</sup>, 5 MJ/m<sup>2</sup>, and 8 MJ/m<sup>2</sup> for the acacia, coconut, and palm kernel char, respectively, is shown in Figures 7(d), 7(e), 7(f).

## 5. Conclusions and Recommendations

**5.1. Conclusions.** The production of an eco-friendly building material with good energy harvesting characteristics from calcined clay reinforced with char (palm kernel shells, coconut shells, and acacia) to investigate its mechanical and thermal properties and to simulate its mechanical and thermal stress distribution is addressed in this study. The study showed that building materials made from calcined clay and char have very good thermal energy harvesting characteristics. The 5 wt.% palm kernel shell char composites recorded the optimum compressive strength of ~4.60 MPa, the highest among the char composite, while the control sample recorded ~7.62 MPa as its compressive strength, and this is above the minimum required compressive strength of bricks for construction. These values are higher than the minimum required compressive strength for building bricks. TGA results show that the composites have high thermal stability at high temperatures, and the simulation results show that the composites that contain char help attain thermal comfort in rooms.

### Data Availability

The data used to support the findings of this study are available from the corresponding author upon request.

### Conflicts of Interest

The authors declare that there are no conflicts of interest.

### Acknowledgments

The authors acknowledge the BANGA-Africa program of the University of Ghana and the Institute of Industrial Research (IIR), Council for Scientific and Industrial Research (CSIR), Ghana, for their assistance.

### References

- [1] Ł. Amanowicz, K. Ratajczak, and E. Dudkiewicz, "Recent advancements in ventilation systems used to decrease energy consumption in buildings—literature review," *Energies*, vol. 16, no. 4, p. 1853, 2023.
- [2] IEA, "Buildings," 2023, <https://www.iea.org/energy-system/buildings>.
- [3] Ł. J. Orman, G. Majewski, N. Radek, and J. Pietraszek, "Analysis of thermal comfort in intelligent and traditional buildings," *Energies*, vol. 15, no. 18, p. 6522, 2022.
- [4] M. A. A. Abdullah, M. A. Razali, R. Abd Rahman et al., "Review of automation and energy monitoring system for air-conditioning and mechanical ventilation (ACMV) in building Malaysia," *Journal of Advanced Mechanical Engineering Applications*, vol. 3, no. 1, pp. 6–15, 2022.
- [5] A. N. Ofori-Boadu, D. Bryant, C. Bock-Hyeng et al., "Physiochemical characterization of agricultural waste biochars for partial cement replacement," *International Journal of Building Pathology and Adaptation*, vol. 40, no. 4, pp. 569–586, 2022.

- [6] L. F. Anzagira, D. Duah, E. Badu, E. K. Simpeh, S. Amos-Abanyie, and A. Marful, "Application of green building concepts and technologies for sustainable building development in Sub-Saharan Africa: the case of Ghana," *Open House International*, vol. 47, no. 3, pp. 408–427, 2022.
- [7] J. Y. Y. Etal, K. Jeong, and D. Lee, "Development of 3D concrete extrusion nozzle for producing free-form concrete panels," *Turkish Journal of Computer and Mathematics Education (TURCOMAT)*, vol. 12, no. 6, pp. 427–436, 2021.
- [8] N. Bassim Frahat, M. Amin, A. Mohamed Heniegal, and O. Mohamed Omar Ibrahim, "Optimizing microencapsulated PCM ratios of sustainable cement mortar for energy savings in buildings," *Construction and Building Materials*, vol. 391, Article ID 131844, 2023.
- [9] R. Isaksson, M. Rosvall, A. Babaahmadi et al., "Supplementary cementitious materials in building blocks—diagnosing opportunities in sub-saharan Africa," *Sustainability*, vol. 15, no. 7, pp. 5822–5827, 2023.
- [10] Y. Wardeh, E. Kinab, G. Escadeillas, P. Rahme, and S. Ginestet, "Review of the optimization techniques for cool pavements solutions to mitigate urban heat islands," *Building and Environment*, vol. 223, 2022.
- [11] N. Sathiparan and H. T. S. M. De Zoysa, "The effects of using agricultural waste as partial substitute for sand in cement blocks," *Journal of Building Engineering*, vol. 19, pp. 216–227, 2018.
- [12] J. Nilimaa, "Smart materials and technologies for sustainable concrete construction," *Developments in the Built Environment*, vol. 15, Article ID 100177, 2023.
- [13] L. Sucupira and J. Castro-Gomes, "Review of energy harvesting for buildings based on solar energy and thermal materials," *CivilEng*, vol. 2, no. 4, pp. 852–873, 2021.
- [14] A. I. Osman, M. Farghali, Y. Dong et al., "Reducing the carbon footprint of buildings using biochar-based bricks and insulating materials: a review," *Environmental Chemistry Letters*, vol. 22, no. 1, pp. 71–104, 2024.
- [15] S. Barbhuiya, B. Bhusan Das, and F. Kanavaris, "Biochar-concrete: a comprehensive review of properties, production and sustainability," *Case Studies in Construction Materials*, vol. 20, Article ID e02859, 2024.
- [16] M. Legan, A. Ž. Gotvajn, and K. Zupan, "Potential of biochar use in building materials," *Journal of Environmental Management*, vol. 309, Article ID 114704, 2022.
- [17] A. Khitab, S. Ahmad, R. A. Khan et al., "Production of biochar and its potential application in cementitious composites," *Crystals*, vol. 11, no. 5, p. 527, 2021.
- [18] S. Wijitkosum and P. Jiwonk, "Elemental composition of biochar obtained from agricultural waste for soil amendment and carbon sequestration," *Applied Sciences*, vol. 9, no. 19, p. 3980, 2019.
- [19] G. Chen, F. Li, P. Jing, J. Geng, and Z. Si, "Effect of pore structure on thermal conductivity and mechanical properties of autoclaved aerated concrete," *Materials*, vol. 14, no. 2, pp. 339–428, 2021.
- [20] S. Praneeth, L. Saavedra, M. Zeng, B. K. Dubey, and A. K. Sarmah, "Biochar admixed lightweight, porous and tougher cement mortars: mechanical, durability and micro computed tomography analysis," *Science of the Total Environment*, vol. 750, Article ID 142327, 2021.
- [21] S. S. Senadheera, S. Gupta, H. W. Kua et al., "Application of biochar in concrete—a review," *Cement and Concrete Composites*, vol. 143, Article ID 105204, 2023.
- [22] G. O. Akintola, F. Amponsah-Dacosta, and S. E. Mhlongo, "Geotechnical evaluation of clayey materials for quality burnt bricks," *Heliyon*, vol. 6, no. 12, Article ID e05626, 2020.
- [23] P. M. Hernandez and G. B. Estores, "Finite element analysis on the effect of concrete bridging on thermal conductivity of sandwich (insulated) precast wall panels," *Civil Engineering and Architecture*, vol. 12, no. 1, pp. 375–390, 2024.
- [24] I. P. Sfikas, J. Ingham, and J. Baber, "Simulating thermal behaviour of concrete by FEA: state-of-the-art review," *Proceedings of the Institution of Civil Engineers-Construction Materials*, vol. 171, no. 2, pp. 59–71, 2018.
- [25] M. Asrardel, Á. Muelas, T. Poonawala, and J. Ballester, "Impact of heat transfer due to fiber conduction, radiation and convection on the interpretation of experiments with isolated droplets," *Combustion and Flame*, vol. 263, Article ID 113384, 2024.
- [26] M. Suleman and P. Gas, "Analytical, experimental and computational analysis of heat released from a hot mug of tea coupled with convection, conduction, and radiation thermal energy modes," *International Journal of Heat and Technology*, vol. 42, no. 2, pp. 359–372, 2024.
- [27] R. N. Konduru, O. Farges, V. Schick, P. Hairy, Y. Gaillard, and G. Parent, "Experimental and numerical investigation of porous heat exchangers with Kelvin cell structured foam at high temperatures: coupled conduction-convection and radiation heat transfer," *International Journal of Heat and Mass Transfer*, vol. 224, Article ID 125253, 2024.
- [28] R. S. C. Davuluri, R. Fu, K. A. Tagavi, and A. Martin, "Fully coupled material response and internal radiative heat transfer for 3D heat shield modeling," *Journal of Thermophysics and Heat Transfer*, vol. 1–16, no. 4, 2023.
- [29] T. Esence, A. Bruch, J. F. Fourmigué, and B. Stutz, "A versatile one-dimensional numerical model for packed-bed heat storage systems," *Renewable Energy*, vol. 133, pp. 190–204, 2019.
- [30] I. Sarbu and A. Dorca, "Review on heat transfer analysis in thermal energy storage using latent heat storage systems and phase change materials," *International Journal of Energy Research*, vol. 43, no. 1, pp. 29–64, 2019.
- [31] M. M. Peiravi and J. Alinejad, "Hybrid conduction, convection and radiation heat transfer simulation in a channel with rectangular cylinder," *Journal of Thermal Analysis and Calorimetry*, vol. 140, no. 6, pp. 2733–2747, 2020.
- [32] V. Chandrakar, J. R. Senapati, and A. Mohanty, "Conjugate heat transfer due to conduction, natural convection, and radiation from a vertical hollow cylinder with finite thickness," *Numerical Heat Transfer, Part A: Applications*, vol. 79, no. 6, pp. 463–487, 2021.
- [33] C. P. Kothandaraman, *Fundamentals of Heat and Mass Transfer*, New Age International Limited, New Delhi, India, 3rd edition, 2006.
- [34] M. Dziegielewski, R. Korycki, H. Szafrńska, and M. Barbuski, "Numerical modeling of the thermal insulating properties of space suits," *Materials*, vol. 17, no. 3, p. 648, 2024.
- [35] R. Fernandez, F. Martirena, and K. L. Scrivener, "The origin of the pozzolanic activity of calcined clay minerals: a comparison between kaolinite, illite and montmorillonite," *Cement and Concrete Research*, vol. 41, no. 1, pp. 113–122, 2011.
- [36] M. Bediako, S. K. Gawu, A. A. Adjaottor, J. Solomon Ankrah, and E. Atiemo, "Analysis of co-fired clay and palm kernel shells as a cementitious material in Ghana," *Case Studies in Construction Materials*, vol. 5, pp. 46–52, 2016.

- [37] M. A. Harech, M. Mesnaoui, Y. Abouliatim et al., "Effect of temperature and clay addition on the thermal behavior of phosphate sludge," *Boletín de la Sociedad Española de Cerámica y Vidrio*, vol. 60, no. 3, pp. 194–204, 2021.
- [38] A. G. Chetverikova, O. N. Kanygina, V. N. Makarov, V. L. Berdinskiy, and M. M. Seregin, "Thermostimulated crystal structure transformation of the polymineral clay submicron particles," *Cerâmica*, vol. 68, no. 388, pp. 441–449, 2022.
- [39] S. Basak, S. Barma, S. Majumdar, and S. Ghosh, "Silane-modified bentonite clay-coated membrane development on ceramic support for oil/water emulsion separation using tuning of hydrophobicity," *Colloids and Surfaces A: Physicochemical and Engineering Aspects*, vol. 681, Article ID 132812, 2024.
- [40] V. D. Pinheiro, J. Alexandre, G. D. C. Xavier, M. T. Marvila, S. N. Monteiro, and A. R. G. de Azevedo, "Methods for evaluating pozzolanic reactivity in calcined clays: a review," *Materials*, vol. 16, no. 13, p. 4778, 2023.
- [41] B. Kwakye-awuah, E. Von-kiti, I. Nkrumah, B. Sefa-ntiri, and C. D. Williams, "Synthesis of zeolites from bauxite and kaolin: effect of synthesis parameters on competing phases," *London United Kingdom*, vol. 20, 2018.
- [42] D. Akolekar, A. Chaffee, and R. F. Howe, "The transformation of kaolin to low-silica X zeolite," *Zeolites*, vol. 19, no. 5–6, pp. 359–365, 1997.
- [43] S. A. Kovo, *Development of Zeolites and Zeolite Membranes from Ahoko Nigerian Kaolin*, The University of Manchester, England, UK, 2011.
- [44] H. Bu, Y. Wei, C. Liu, D. Liu, D. Tan, and H. Liu, "Effects of illite-smectite clay minerals on the thermal evolution of aliphatic organic matter-clay complexes: a study with thermogravimetry coupled with Fourier transform infrared spectroscopy (TG-FTIR)," *Journal of Thermal Analysis and Calorimetry*, vol. 148, no. 3, pp. 741–752, 2022.
- [45] P. E. Grattan-Bellew, "Microstructural investigation of deteriorated Portland cement concretes," *Construction and Building Materials*, vol. 10, no. 1, pp. 3–16, 1996.
- [46] M. E. Gomah, G. Li, A. A. Omar, M. L. Abdel Latif, C. Sun, and J. Xu, "Thermal-induced microstructure deterioration of Egyptian granodiorite and associated physico-mechanical responses," *Materials*, vol. 17, no. 6, p. 1305, 2024.
- [47] K. U. Hess, J. E. K. Schawe, M. Wilding et al., "Glass transition temperatures and crystallization kinetics of a synthetic, anhydrous, amorphous calcium-magnesium carbonate," *Philosophical Transactions Series A, Mathematical, physical, and engineering sciences*, vol. 381, no. 2258, Article ID 20220356, 2023.
- [48] Q. Liang, D. Pan, and X. Zhang, "Construction and application of biochar-based composite phase change materials," *Chemical Engineering Journal*, vol. 453, Article ID 139441, 2023.
- [49] X. Lin, W. Li, Y. Guo, W. Dong, A. Castel, and K. Wang, "Biochar-cement concrete toward decarbonisation and sustainability for construction: characteristic, performance and perspective," *Journal of Cleaner Production*, vol. 419, Article ID 138219, 2023.
- [50] F. C. R. Lopes and K. Tannous, "Coconut fiber pyrolysis: specific heat capacity and enthalpy of reaction through thermogravimetry and differential scanning calorimetry," *Thermochimica Acta*, vol. 707, Article ID 179087, 2022.
- [51] B. Miguiri, I. Wirba, J. T. Zaida, A. Vondou, and R. Mouanguel, "Thermal characterization of local tropical woods in view of their valorization," *Article in Journal of Materials and Environmental Sciences*, vol. 2020, no. 5, pp. 759–771, 2020.
- [52] R. S. Fono-Tamo, O. A. Koya, R. S. Fono-Tamo, and O. A. Koya, "Characterisation of pulverised palm kernel shell for sustainable waste diversification," 2013, <http://www.ijser.org>.
- [53] S. Gupta, H. W. Kua, and S. D. Pang, "Biochar-mortar composite: manufacturing, evaluation of physical properties and economic viability," *Construction and Building Materials*, vol. 167, pp. 874–889, 2018.
- [54] J. Junior, A. K. Saha, P. K. Sarker, and A. Pramanik, "Workability and flexural properties of fibre-reinforced geopolymer using different mono and hybrid fibres," *Materials*, vol. 14, no. 16, p. 4447, 2021.
- [55] M. Gupta, J. Yang, and C. Roy, "Specific heat and thermal conductivity of softwood bark and softwood char particles," *Fuel*, vol. 82, no. 8, pp. 919–927, 2003.